

## Equatorial scintillation and systems support

K. M. Groves,<sup>1</sup> S. Basu,<sup>1</sup> E. J. Weber,<sup>1</sup> M. Smitham,<sup>1</sup> H. Kuenzler,<sup>1</sup>  
C. E. Valladares,<sup>2</sup> R. Sheehan,<sup>2</sup> E. MacKenzie,<sup>2</sup> J. A. Secan,<sup>3</sup>  
P. Ning,<sup>4</sup> W. J. McNeill,<sup>5</sup> D. W. Moonan,<sup>5</sup> and M. J. Kendra<sup>5</sup>

**Abstract.** The need to nowcast and forecast scintillation for the support of operational systems has been recently identified by the interagency National Space Weather Program. This issue is addressed in the present paper in the context of nighttime irregularities in the equatorial ionosphere that cause intense amplitude and phase scintillations of satellite signals in the VHF/UHF range of frequencies and impact satellite communication, Global Positioning System navigation, and radar systems. Multistation and multifrequency satellite scintillation observations have been used to show that even though equatorial scintillations vary in accordance with the solar cycle, the extreme day-to-day variability of unknown origin modulates the scintillation occurrence during all phases of the solar cycle. It is shown that although equatorial scintillation events often show correlation with magnetic activity, the major component of scintillation is observed during magnetically quiet periods. In view of the day-to-day variability of the occurrence and intensity of scintillating regions, their latitude extent, and their zonal motion, a regional specification and short-term forecast system based on real-time measurements has been developed. This system, named the Scintillation Network Decision Aid, consists of two latitudinally dispersed stations, each of which uses spaced antenna scintillation receiving systems to monitor 250-MHz transmissions from two longitudinally separated geostationary satellites. The scintillation index and zonal irregularity drift are processed on-line and are retrieved by a remote operator on the Internet. At the operator terminal the data are combined with an empirical plasma bubble model to generate three-dimensional maps of irregularity structures and two-dimensional outage maps for the region.

## Introduction

Even after two decades of intensive investigations by theoretical and experimental geophysicists, the space-time variability of nighttime *F*-region irregularities remains an outstanding problem [Basu and Basu, 1985, and references therein; Basu *et al.*, 1996]. This problem is of serious concern to systems engineers since it is well-known that these irregularities cause amplitude and phase scintillation of satellite signals. Scintillations affect satellite communication and navigation systems in various ways [Aarons and Basu, 1994; Basu *et al.*, 1995]. For example, amplitude scintillations induce signal fading, and when the

depth of fading exceeds the fade margin of a receiving system, message errors in satellite communication systems are encountered. In Global Positioning System (GPS) navigation systems, amplitude scintillation may cause data loss and cycle slips. Phase scintillations, if severe, may sufficiently stress phase-lock loops in GPS receivers such that loss of phase lock is experienced. Overall, equatorial scintillation is often sufficiently intense to disable many communication and navigation systems.

The users need forecasts of equatorial scintillation to make sure that the outages are caused by scintillation and not by system failures and also for developing alternate methods of communication and navigation. This need has been emphasized recently in the interagency (Department of Defense, National Science Foundation, Department of Commerce, NASA, Department of Interior, and Department of Energy) National Space Weather Program (NSWP) Strategic Plan. We should note that the climatology of equatorial scintillation is fairly well established [Basu *et al.*, 1988; Aarons, 1993], and its features can be reproduced by the use of the recently upgraded

<sup>1</sup> Phillips Laboratory, Hanscom Air Force Base, Massachusetts.

<sup>2</sup> Institute for Scientific Research, Boston College, Newton, Massachusetts.

<sup>3</sup> Northwest Research Associates, Bellevue, Washington.

<sup>4</sup> Keo Consultants, Brookline, Massachusetts.

<sup>5</sup> Radex Incorporated, Bedford, Massachusetts.

Copyright 1997 by the American Geophysical Union.

Paper number 97RS00836.

0048-6604/97/97RS-00836\$11.00

scintillation model WBMOD [Secan *et al.*, 1995]. However, we are not able to provide scintillation weather information due to the extreme temporal and spatial variability of scintillation.

Theoretical and experimental studies have revealed that at least two types of nighttime *F*-region irregularities arise in the equatorial region, namely, those related to plasma bubbles [Haerendel, 1973; McClure *et al.*, 1977; Scannapieco and Ossakow, 1976; Ossakow, 1981; Kelley, 1989] and those called the bottomside sinusoidal (BSS) irregularities, or simply bottomside irregularities [Valladares *et al.*, 1983]. The plasma bubbles as discussed in the quoted references originate in the bottomside *F* region and become highly structured as they penetrate to altitudes exceeding 1000 km above the magnetic equator. These are widely recognized as plumes on radar backscatter maps [Woodman and La Hoz, 1976; Tsunoda, 1981; Tsunoda *et al.*, 1982]. These bubbles extended in altitude map out along the magnetic field to anomaly locations of 15°N and 15°S magnetic latitudes. The magnitude of scintillation, however, varies with magnetic latitude since the background ionization density is minimum at the magnetic equator and maximum around the anomaly locations. On the other hand, the bottomside irregularities with limited altitude extent are confined over a relatively narrow latitude range around the magnetic equator.

In this paper we shall first contrast the features of scintillation statistics at the magnetic equator and the equatorial anomaly regions at both L band and 250-MHz. We shall indicate the existence of a localized source of 250-MHz scintillation near the magnetic equator. We shall discuss the spatial and temporal variability of 250-MHz scintillation as well as the features of the ionospheric motion. We shall then present the Scintillation Network Decision Aid (SCINDA) that has been recently developed at the Phillips Laboratory to provide real-time regional specification and forecasting of equatorial scintillation at 250 MHz.

## Results and Discussion

### Geometry of Observing Stations

Figure 1 shows the locations of the ground stations that provided scintillation data used in this study. It may be noted that the station at Huancayo, Peru, is located near the magnetic equator, whereas Ascension Island is situated close to the crest of the equatorial anomaly at a magnetic latitude of about

15°S. A station near the magnetic equator, such as Huancayo, detects a larger number of scintillation events, at least at low frequencies, since the equatorial irregularities originate at the magnetic equator. On the other hand, stations near the crests of the equatorial anomaly detect most intense scintillation events, since the ambient ionization density attains high values during the early evening hours when the irregularities occur. These two stations have provided much of the long-term scintillation data at 250 MHz and L band. More recently, scintillation measurements near the magnetic equator are being made at Ancon, Peru, instead of at Huancayo. Figure 1 shows that the station receives 250-MHz signals from two geostationary satellites in the west and the east, and the intersection of these propagation paths with the ionospheric height of 350 km, namely, the subionospheric points, are indicated by I1 and I2, respectively. The set of three parallel lines near the Ancon station illustrate the projections of the Earth's magnetic field lines mapped from apex altitudes of 400, 600, and 800 km down to 200 km altitude above Ancon. To the south of Ancon, the station at Antofagasta, Chile, at a magnetic latitude of 11°S, also records 250-MHz signals from the same two geostationary satellites that are monitored at Ancon. The 350-km subionospheric points for the west and the east geostationary satellites are indicated by I3 and I4, respectively. The thin parallel lines in the vicinity of Antofagasta again illustrate the projections of the Earth's magnetic field mapped from apex altitudes of 400, 600, and 800 km to 200 km altitude above this station. Considering the magnetic field projections, we find that an altitude of 200 km above Antofagasta and Ascension Island maps along magnetic field lines to the magnetic equator to altitudes of 400 and 800 km, respectively.

The stations at Ancon, Antofagasta, and Ascension Island deploy receivers that acquire 250-MHz and L-band signals from geostationary satellites and sample the detected signals at 50 Hz. The signals are processed on-line to determine at 90-s intervals the scintillation index  $S_4$ , which is defined as the standard deviation of the normalized signal intensity,  $I/\langle I \rangle$ . In addition, the power spectrum of scintillation by the fast Fourier transform (FFT) and cumulative amplitude distribution function are also processed. At Ancon and Antofagasta, the scintillation data are acquired by receivers with antennas spaced in the magnetic east-west direction. These autocorrelation and cross-correlation functions of the spaced antenna

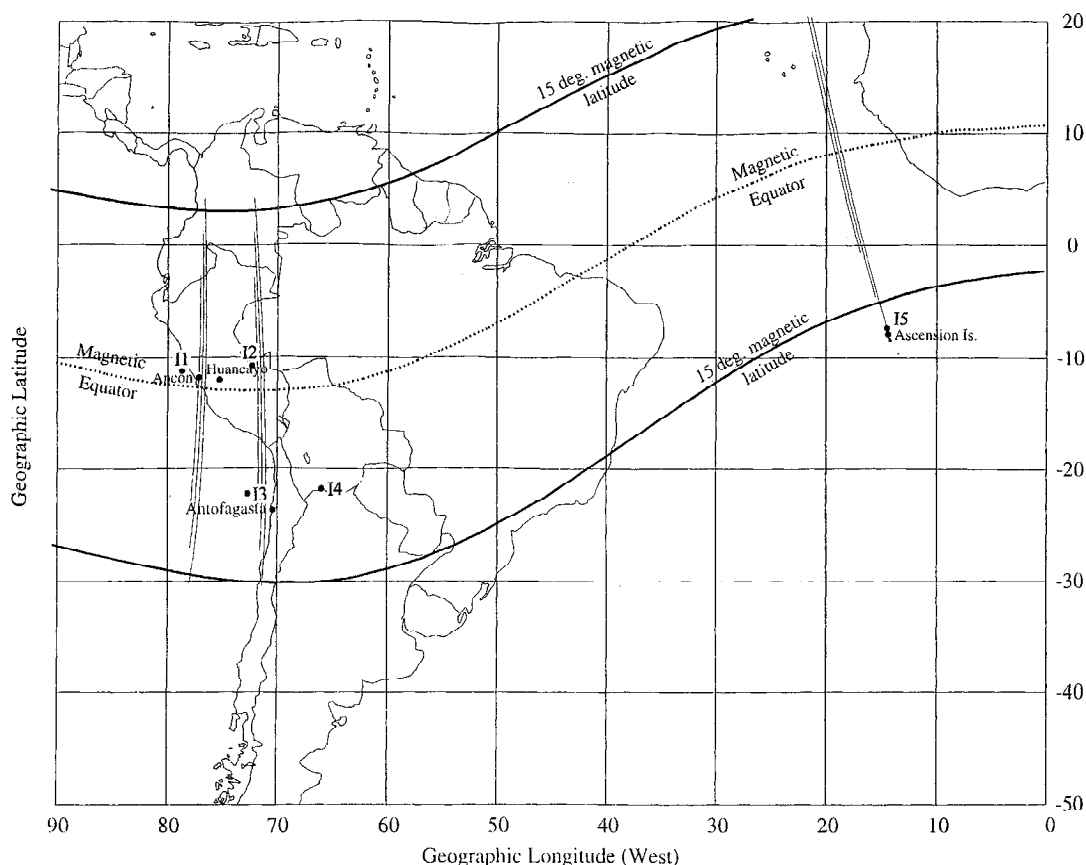


**Figure 1.** Locations of the ground stations at Huancayo, Ancon, and Ascension Island which performed scintillation observations. The 350-km subionospheric points are indicated: I1 and I2, for the west and the east satellite observations, respectively, from Ancon; I3 and I4, corresponding to Antofagasta; and I5 for east satellite observations from Ascension Island. The sets of three parallel lines near Ancon, Antofagasta, and Ascension Island, displaced for clarity, represent projections of magnetic field lines with apex altitudes of 400, 600, and 800 km which are mapped to 200 km altitude.

data are processed to determine the east-west drift speed of the irregularities at both sites.

#### Scintillation Statistics at the Magnetic Equator and the Equatorial Anomaly

As mentioned earlier, the bubble-related scintillation is expected to be extended in latitude due to the magnetic field alignment of the bubbles and to be most intense near the equatorial anomaly. The latitude variation of this type of scintillation is best studied at gigahertz frequencies which do not readily get saturated by these intense events. Figure 2 shows the variation in the occurrence of equatorial scintillation at 1.54 GHz during 1986–1989. The statistics have been established for the time interval of 2000–2400 LT, when L-band scintillations usually occur,

and for three increasing levels of scintillation corresponding to signal fading of 2, 10, and 20 dB. The top panel shows the monthly occurrence statistics for Ascension Island, and the middle panel shows them for Huancayo. The bottom panel shows the variation of the sunspot number during 1986–1989. An inspection of the diagram shows that both stations encounter increased scintillation activity as the sunspot number increases from the solar minimum year of 1987 and approaches the solar maximum. Before we discuss the latitude variation of scintillation, we should note that Huancayo and Ascension, though separated in longitude, belong to the longitude sector with similar seasonal variation. The characteristic seasonal variation in this sector, namely, minimum scintillation activity during May–August [Aarons, 1993], is illus-

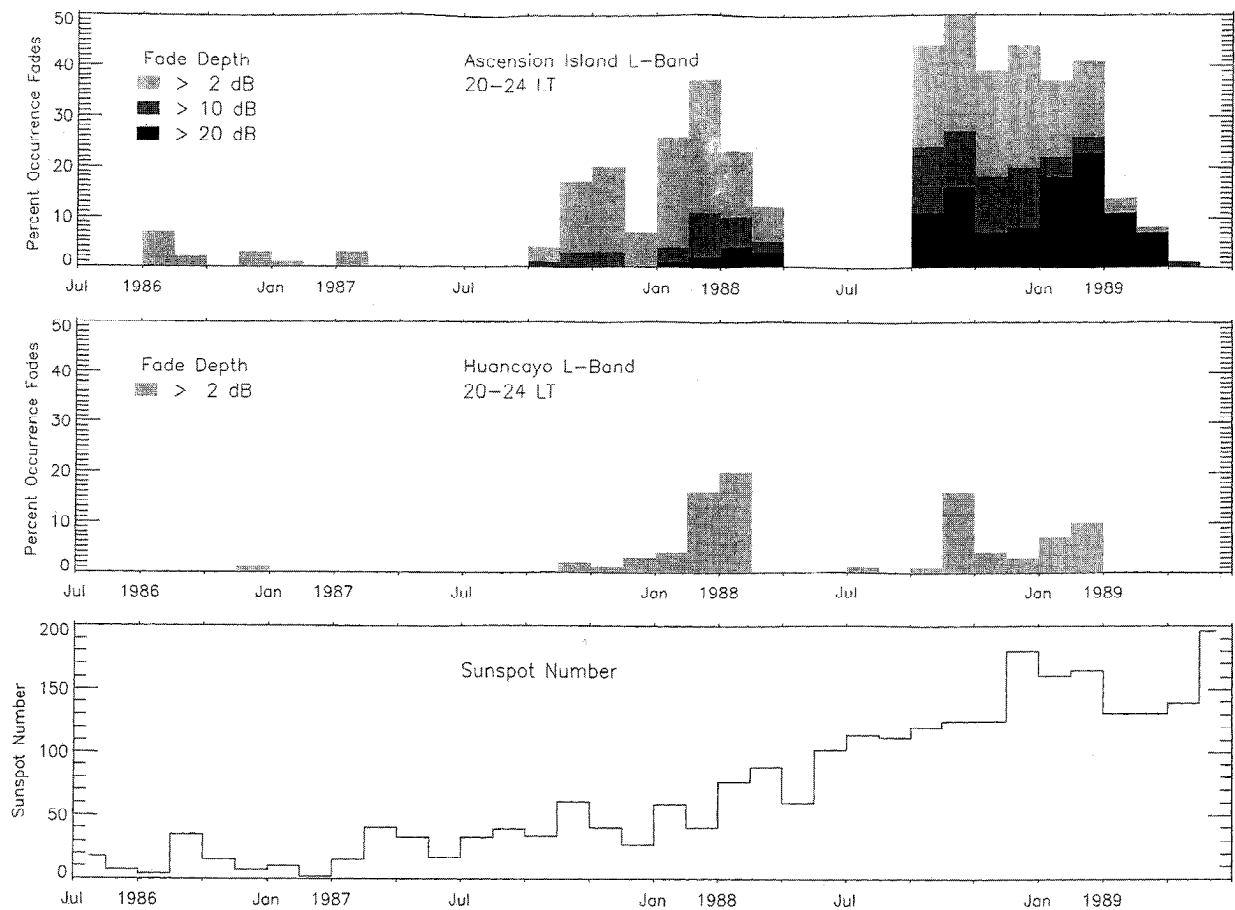


**Figure 2.** The occurrence statistics of L-band (1.54 GHz) scintillation, for fades exceeding 2, 10, and 20 dB. The top panel shows the statistics for Ascension Island near the crest of the equatorial anomaly during 1986–1988. The middle panel shows that only 2 dB statistics can be obtained at Huancayo for the same period. The bottom panel shows the variation of sunspot number.

trated in the top two panels. The most distinguishing feature of Figure 2, however, is the pronounced variation of scintillation activity between the magnetic equator and the crest of the equatorial anomaly. At Huancayo, even during the solar maximum period, fading depths as low as 2 dB do not occur more than 20% of the time. On the other hand, at Ascension Island, similar levels of occurrence are attained at a much higher depth of fading, namely, 20 dB. The fading depths of 2 and 20 dB correspond to scintillation indices  $S_4 = 0.18$  and  $0.89$ , respectively. The factor of 5 enhancement of scintillation at Ascension near the equatorial anomaly may be accounted for by considering that the  $F$ -region ionization density at Ascension is enhanced by a factor of 5 above the magnetic equator and that the irregularity amplitude

is preserved between the magnetic equator and the equatorial anomaly. Such enhancements of  $F$ -region ionization density at the anomaly location as compared with that at the magnetic equator are typical during the postsunset period.

#### Scintillations Under Magnetically Quiet and Active Conditions

In Figure 2 we grouped together scintillation data for all magnetic conditions. In order to investigate the dependence on magnetic activity, we divide the data set shown in the top panel of Figure 2 in two groups, namely, under magnetically quiet ( $Kp = 0-3$ ) and active ( $Kp = 3^+-9$ ) periods. In Figure 3 we illustrate the occurrence statistics of 1.54-GHz scintillation as recorded at Ascension Island for magnetically quiet

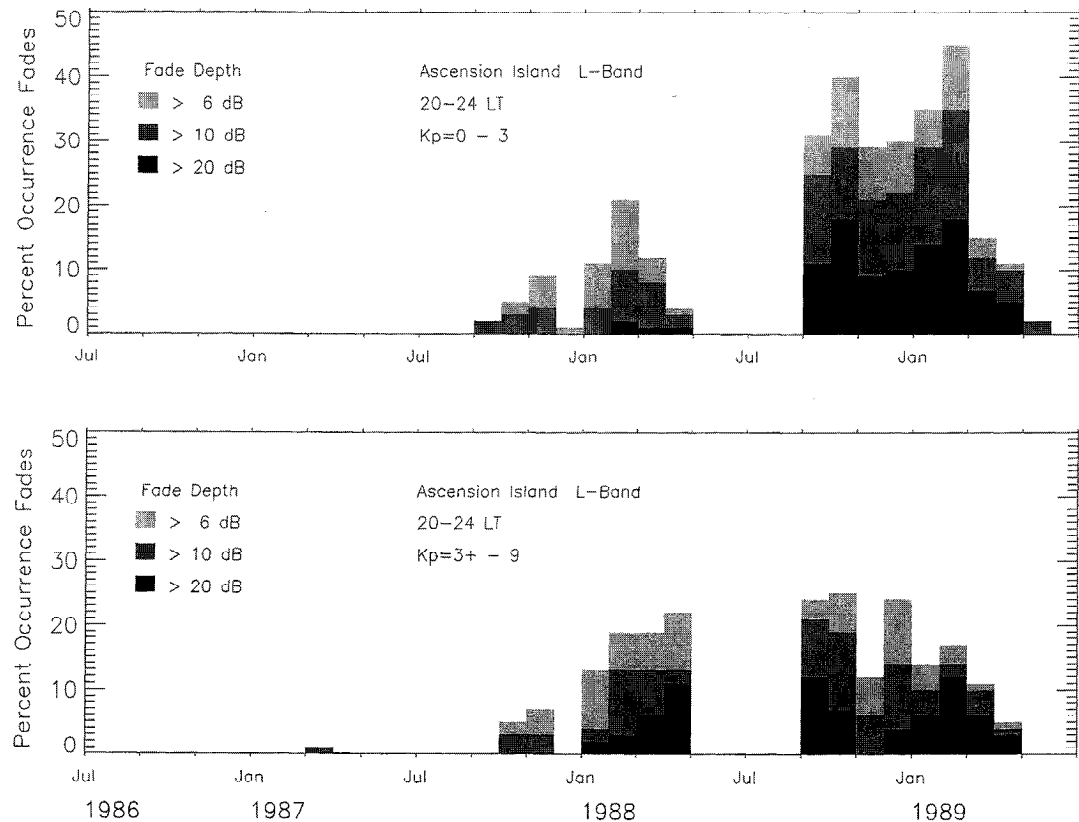


**Figure 3.** The occurrence statistics of L-band scintillation at Ascension Island during magnetically quiet ( $K_p = 0-3$ ) and active ( $K_p = 3^+-9$ ) conditions.

and active conditions. The diagram corresponds to 2000–2400 LT when L-band scintillations usually occur. The top panel refers to magnetically quiet conditions ( $K_p = 0-3$ ) and the bottom panel to magnetically active conditions ( $K_p = 3^+-9$ ). The figure shows that even though scintillations occur during magnetically active periods [Aarons, 1991], a major component of scintillation is associated with magnetically quiet conditions. The top panel shows that during magnetically quiet periods, 20-dB fades are encountered 20% of the time, a level of activity that seriously impacts robust communication and navigation systems. Under magnetically quiet conditions the postsunset enhancement of the eastward electric field [Heelis *et al.*, 1974; Rishbeth, 1971a, b, 1981; Farley *et al.*, 1986; Fejer, 1991; Fejer *et al.*, 1991; Haerendel and Eccles, 1992; Basu *et al.*, 1996] is considered to be a major factor needed to destabilize the ionosphere [Haerendel, 1973; Ossakow, 1981]. The complex thermosphere-ionosphere interactions that generate the postsunset electric field during magnet-

ically quiet conditions remain unresolved and unpredictable. In addition to the above, the stabilizing influence of the meridional wind [Maruyama and Matuura, 1984] cannot be predicted either.

#### Latitude Extent of Equatorial Scintillation

We had mentioned earlier that bubble-related scintillations are extended in latitude in view of their field alignment and altitude extent above the magnetic equator. On the other hand, we often encounter irregularities with limited altitude extent above the magnetic equator [Aarons *et al.*, this issue]. The bottomside sinusoidal irregularities (BSS) with steep irregularity power spectrum and correlation lengths of the order of 1 km belong to this class [Valladares *et al.*, 1983]. However, in addition to BSS, which occur during the solstices, we often encounter, in other seasons, scintillation events that are limited in latitude. In Figure 4 we contrast the occurrence statistics of 250-MHz scintillation at Ascension Island (top panel) near the crest of the equatorial anomaly with

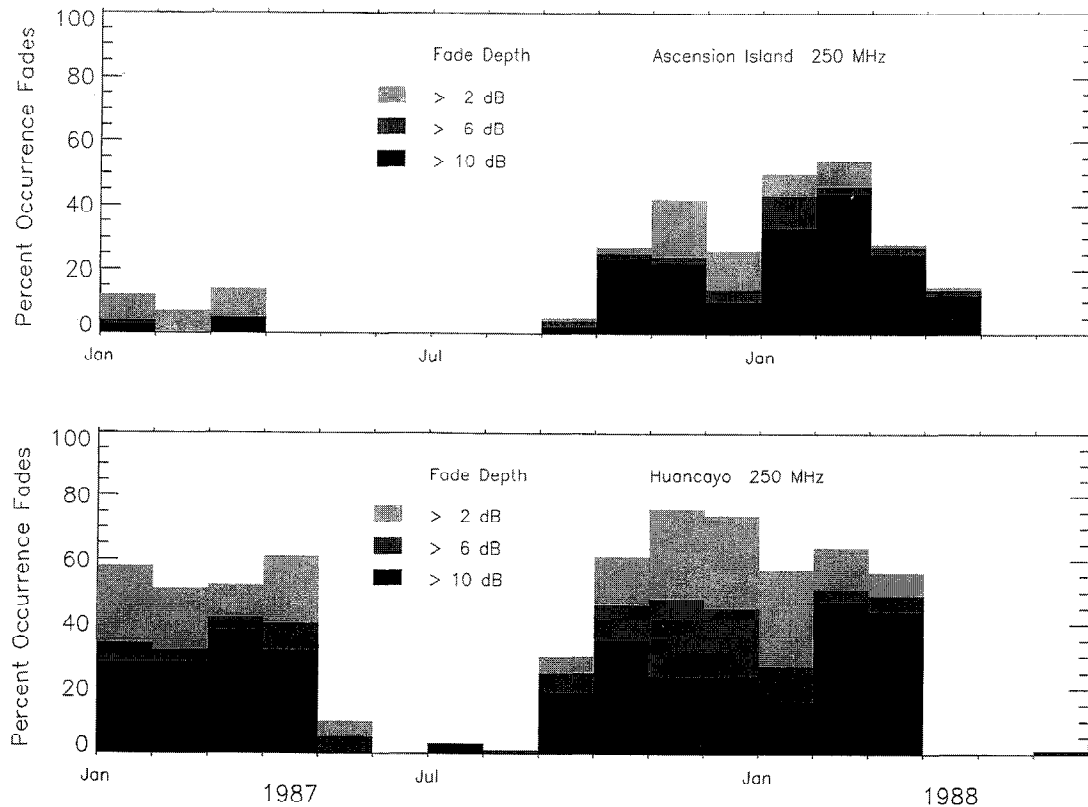


**Figure 4.** The occurrence statistics of 250-MHz scintillation at Ascension Island and Huancayo. This figure illustrates higher occurrence of 250-MHz scintillation at Huancayo near the magnetic equator.

that observed at Huancayo (bottom panel) near the magnetic equator. The occurrence statistics are shown for three progressively increasing levels of scintillation, corresponding to signal fadings exceeding 2, 6, and 10 dB. Referring to the bottom panel of Figure 2, we find that during the time period covered by Figure 4, the sunspot number increased from a minimum to a moderate level. This explains the overall increase of scintillation during 1988. The most interesting feature of this figure is related to the fact that the scintillation activity at 250 MHz is more prevalent near the magnetic equator (Huancayo) as compared with that at Ascension Island. This is more marked during early 1987 when the sunspot number was low, indicative of the fact that during the solar minimum the irregularity structure or the scintillation belt does not extend as far poleward as Ascension Island. During the period September 1987 to March 1988, higher scintillation occurrence near the equator is especially marked at lower levels of scintillation. This establishes that there is indeed a class of equa-

torial irregularities of limited thickness that can map over a narrow-latitude belt around the magnetic equator. These are well detected by 250-MHz observations but usually too weak to be detected by L-band scintillation measurements, as indicated by Figure 2.

We shall now illustrate the variability of the latitude extent of the irregularities with two specific data samples. Figure 5a illustrates a 250-MHz scintillation event that extended from Ancon, Peru, to Antofagasta, Chile. From Figure 1 we may note that Ancon is near the magnetic equator and Antofagasta has a magnetic latitude of  $11^{\circ}\text{S}$ . The top two panels show the variation of  $S_4$  index of scintillation at 250 MHz, as recorded at Ancon with a geostationary satellite to the west and to the east of the station, respectively. The abscissa indicates the universal time (UT), which is related to the local time (LT) as  $LT = UT - 5$  hours. The bottom two panels show the corresponding results obtained at Antofagasta, Chile. We may note from the top panel that the scintillation structure detected at Ancon in the west drifted eastward at a

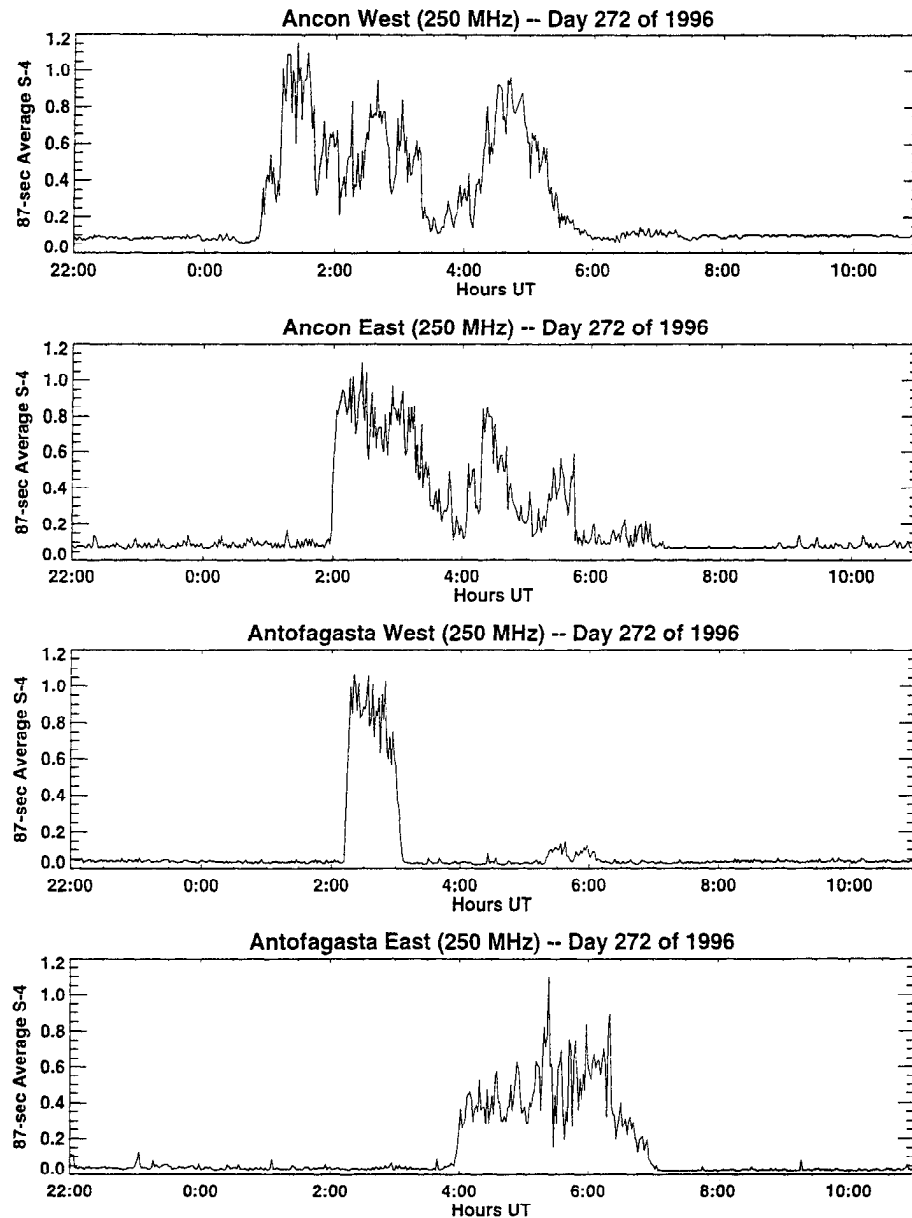


**Figure 5a.** The temporal variation of the  $S_4$  index of scintillation recorded on day 272, 1996, at Ancon by using the west satellite (top panel) and the east satellite (second panel) and at Antofagasta by using the west satellite (third panel) and the east satellite (bottom panel). This figure illustrates that the scintillation structure extended from the magnetic equator to at least  $11^\circ$  magnetic latitude.

speed of  $170 \text{ m s}^{-1}$  and caused scintillation on the east satellite link (second panel) at about 0200 UT. The third panel shows that the Antofagasta station detected scintillations simultaneously with the onset of scintillation in the second panel. This is because the ionospheric intersection of Ancon with the east geostationary satellite and the intersection of Anto-

fagasta with the west satellite lie on the same magnetic flux tube (compare with Figure 1). These observations indicate that the irregularities extended to altitudes of at least 600 km above the magnetic equator at Ancon to be mapped to the subionospheric location of Antofagasta observations at a magnetic latitude of  $10^\circ\text{S}$ . Figure 5b illustrates that 2 days prior

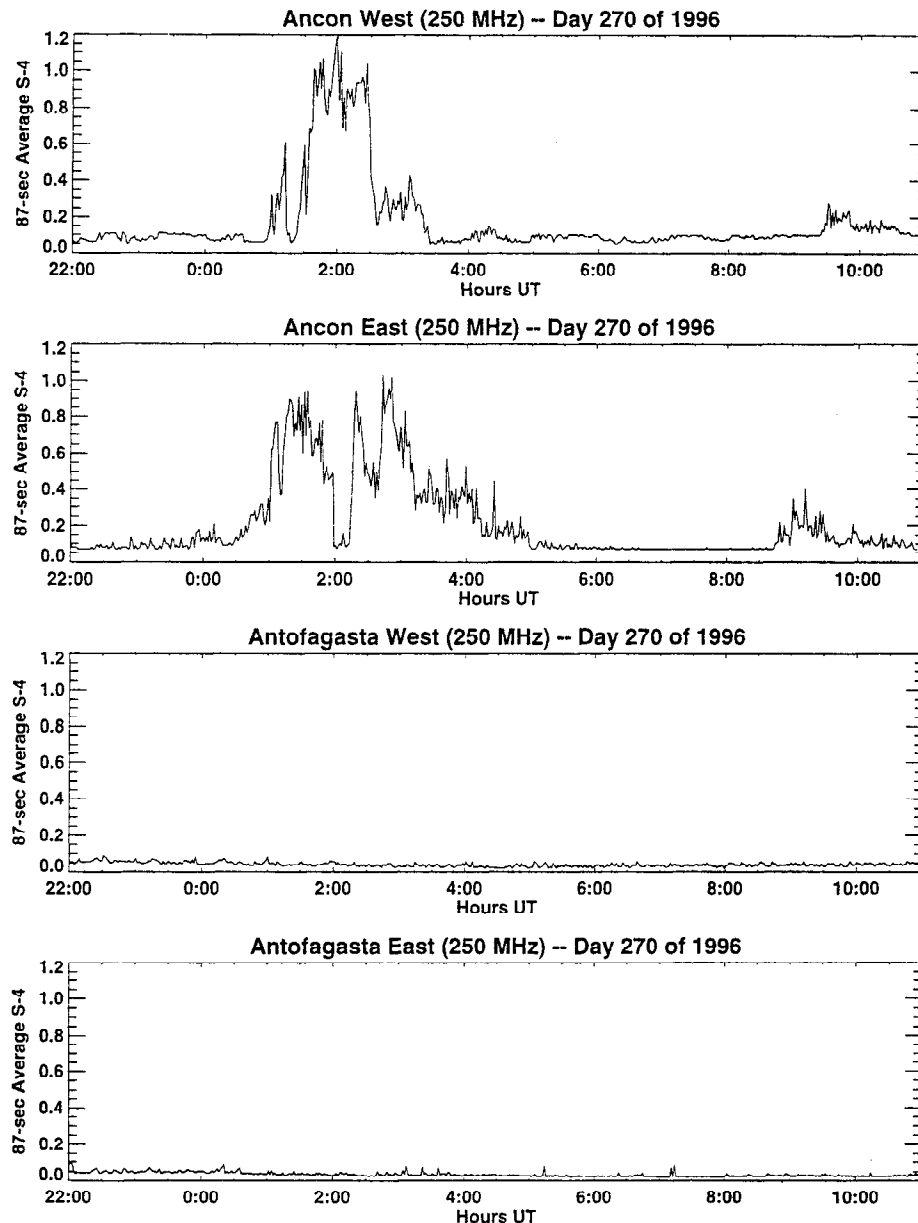


**Figure 5b.** Same as in Figure 5a except for day 270, 1996, when scintillation structures did not extend to Chile.

to the above observations, scintillations were observed at Ancon only and did not extend to Antofagasta. We cannot say exactly how high the irregularity structures extended in altitude above the magnetic equator on this evening, but we know that it remained below 600 km and that the latitude extent was less than  $10^\circ$  magnetic latitude.

These results indicate that plasma bubbles, which

contain the scintillation causing kilometer-scale irregularities, attain varying altitudes on different days. This can be attributed to variations in the vertical rise velocity of plasma bubbles, which have been shown to depend on  $dN/N$ , the fractional plasma density depletion, and  $g/v_{in}$ , the ratio of gravity and the ion-neutral collision frequency [Ossakow and Chaturvedi, 1978; Ott, 1978]. Ossakow and Chaturvedi [1978]



considered nonlinear models of constant-shape bubbles and showed that for all models the rise velocity increases with increasing altitude and/or increasing fractional density depletion, although the exact magnitude depends on the specific shape of the bubble. These authors show that for a cylindrical bubble at an altitude of 350 km, the bubble rise velocity may be as low as  $6 \text{ m s}^{-1}$  for a fractional density depletion of 25% and as high as  $40 \text{ m s}^{-1}$  for 100% depletion. At higher altitudes, such as 450 km, the rise velocities correspond to 30 and  $220 \text{ m s}^{-1}$  for 25% and 100% depletions, respectively. Satellite in situ measurements do indeed show this wide variability of rise velocity in plasma bubbles [McClure *et al.*, 1977]. Since the equatorial *F* region descends in the early evening hours following the prereversal maximum, bubbles with low fractional density depletion having low rise velocity may be stopped from attaining higher altitudes. Thus the variability in fractional density depletion may indeed explain the observed variation in the latitude extent of the irregularities.

### Temporal Variability of Scintillation

Figure 6 illustrates the extreme temporal variability of scintillation. The figure shows the daily variation of the  $S_4$  index of scintillation recorded at Ancon. It indicates that three nights of no scintillation activity were followed by three nights with substantial scintillation. The entire period was magnetically quiet; as such, the extreme variability of scintillation cannot be attributed to a difference in magnetic activity. The following week started with five nights of scintillation activity that were followed by two nights of no activity. Thus some nights remain totally benign even though the February–March period corresponds to the season of high scintillation occurrence. As mentioned earlier, the variability of equatorial scintillation under magnetically quiet conditions remains unresolved. The destabilizing and stabilizing roles of several key neutral and plasma parameters have been critically examined by plasma physicists and modelers [Ossakow *et al.*, 1979; Anderson and Haerendel, 1979; Sekar *et al.*, 1994; Crain *et al.*, 1993]. From an observational standpoint, however, the sources of day-to-day variability are yet to be identified. A few crucial parameters, such as neutral winds, which play a major role in determining the equatorial electrodynamics, have not been measured around the sunset period. Although O I 630.0-nm dayglow has been recently measured [Sridharan *et al.*, 1994], neutral wind mea-

surements, during the crucial presunset hours, by optical techniques have not yet been possible.

### Zonal Motion of Scintillating Regions

After sunset the *F*-region dynamo becomes effective, and a vertically downward polarization electric field develops at *F*-region heights [Rishbeth, 1971a, b]. This polarization electric field is responsible for the eastward motion of the ionosphere during the night. Owing to this zonal motion, scintillating regions are observed to move from the west to the east. Spaced antenna scintillation measurements are being routinely performed at Ancon, Peru [Valladares *et al.*, 1996], as well as at Antofagasta, Chile. We shall examine the characteristic variation of the zonal drift. Under magnetically active conditions, the penetration of the high-latitude electric field and the disturbance dynamo affects the equatorial electrodynamics. As such, we show the statistics of the zonal drift separately for magnetically quiet ( $Kp < 3$ ) and magnetically active ( $Kp > 3$ ) periods.

Figure 7a shows the seasonal variation of the zonal drift obtained under magnetically quiet conditions during the period May 1994 to April 1996. Each data point in the scatter diagram represents a 5-min average of the measured drift, and the open circles denote the hourly median value. An inspection of the figure shows that the zonal irregularity drift is well ordered and eastward except for a few points with westward flows. The relatively sparse data points during May–July arise from the low occurrence of scintillation during these months.

Figure 7b shows the seasonal variation of the zonal drift under magnetically disturbed conditions. Comparing Figures 7a and 7b, we find that in all seasons except May–July the number of data points in Figure 7b is reduced, indicating an overall decrease of scintillation occurrence during magnetically disturbed periods. During May–July, when scintillations are rarely observed at Ancon, magnetic activity is observed to enhance the scintillation occurrence. Further, we may note a preponderance of westward flows during magnetically active conditions due to the effects of the disturbance dynamo electric fields [Fejer, 1991; Fejer *et al.*, 1991]. Valladares *et al.* [1996] have shown that the overall features of the seasonal variation of the zonal plasma drift can be accounted for by considering models of zonal drifts based on zonal neutral wind and integrated Pedersen conductivity. As may be noted from Figures 7a and 7b, there is considerable day-to-day variation of the drift speed,

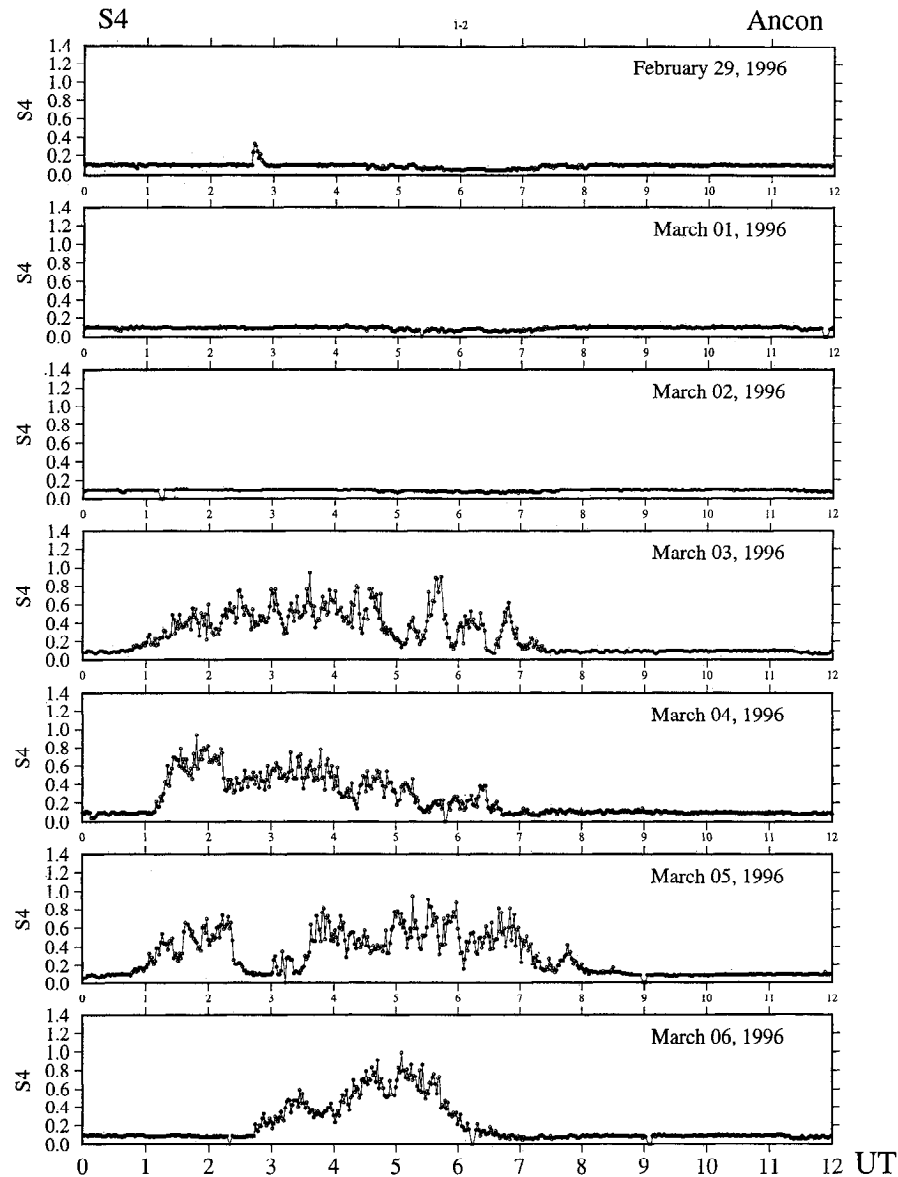


**Figure 6.** The temporal variation of 250-MHz scintillation recorded at Ancon on five successive nights. This figure illustrates the extreme variability of scintillation with three nights of no scintillation followed by four nights of scintillation activity.

and this variability cannot be modeled. As such, accurate predictions of the position of a drifting scintillating region will require simultaneous drift measurements.

#### Scintillation Network Decision Aid (SCINDA)

Because of the variable and unpredictable nature of scintillation occurrence, intensity, and dynamics described above, a system known as the Scintillation

Network Decision Aid (SCINDA) has been developed to provide users with real-time regional specification and short-term forecasts of 250-MHz scintillation. Indeed, a fundamental objective of the SCINDA project has been to distill complex scintillation data sets into simplified, operationally accurate products which can be readily understood by nontechnical users of satellite communications and navigation. The SCINDA system, illustrated schematically in Figure 8,

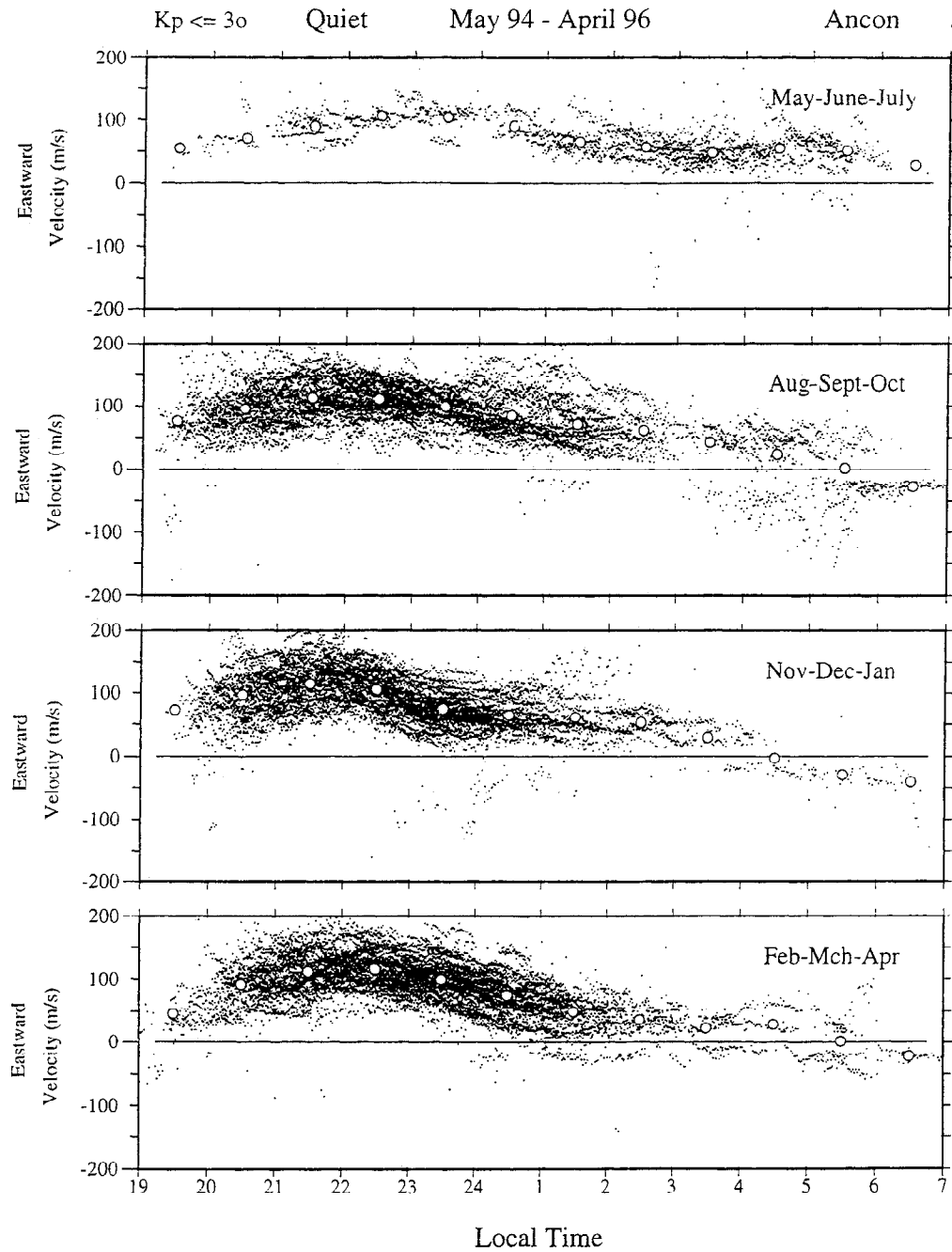


**Figure 7a.** The scatterplot of the east-west irregularity drift measured at Ancon under magnetically quiet ( $K_p < 3$ ) conditions during May–July (top panel), August–October (second panel), November–January (third panel), and February–April (bottom panel). The open circles denote the hourly median values.

consists of a network of ground-based receivers which monitor satellite transmissions and provide scintillation data in near real-time to drive a computer model which integrates the measurements and generates

physically consistent graphical representations of scintillation features. The model is designed to function well with a data stream from a minimum of two ground-based receivers separated in latitude; ideally,

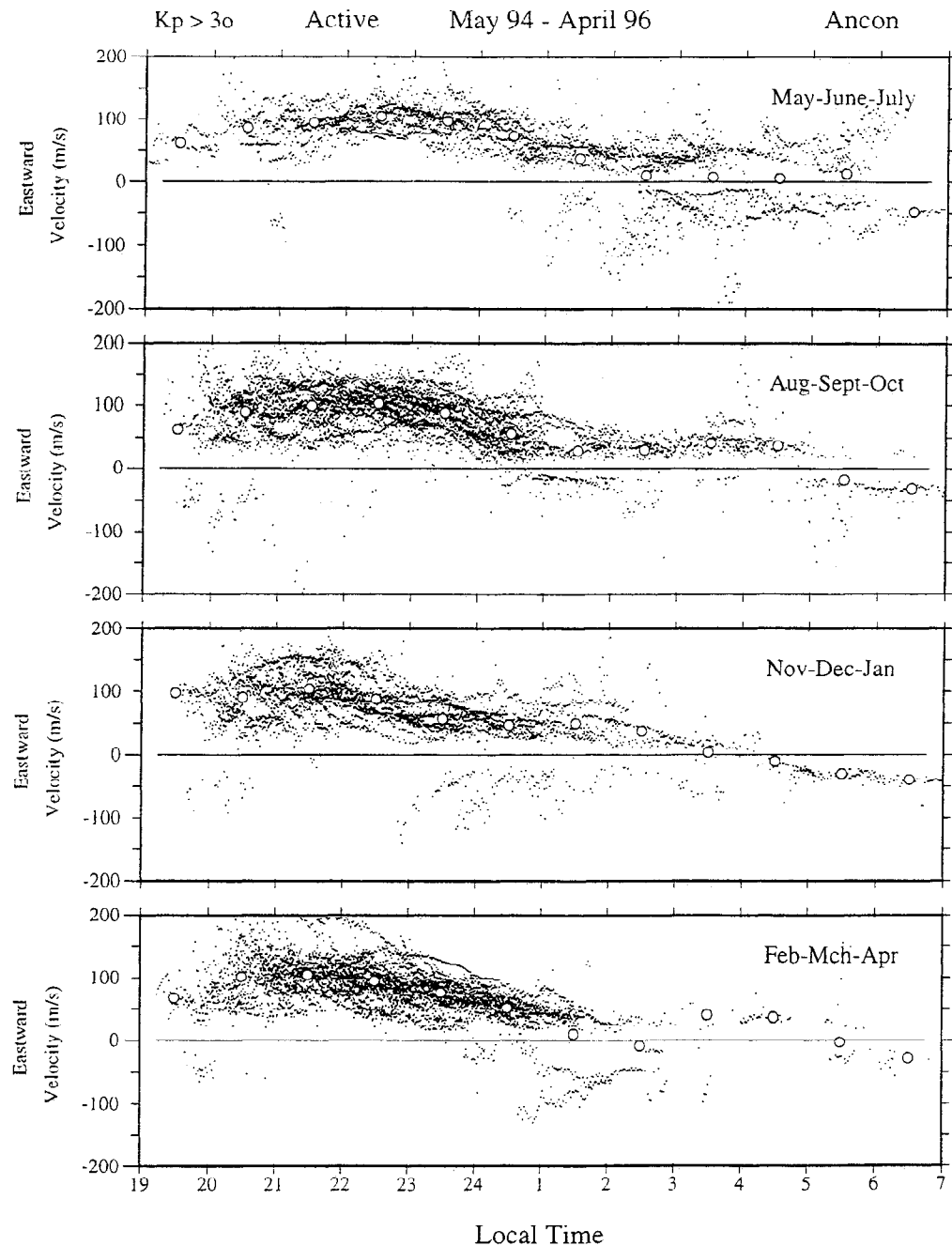


**Figure 7b.** Same as in Figure 7a except for magnetically disturbed ( $Kp > 3$ ) conditions.

one should be situated at the magnetic equator and the other close to an equatorial anomaly crest location, nominally at about  $\pm 15^\circ$  magnetic latitude.

In the current implementation, satellite receiving stations have been established at Ancon, Peru, near the magnetic equator and at Antofagasta, Chile,  $11^\circ$ S

magnetic latitude, as was shown in Figure 1 and described previously. Each station uses spaced antenna scintillation receiving systems to monitor 250-MHz transmissions from two geostationary satellites, one in the west and the other in the east. The receiving systems perform on-line processing of the

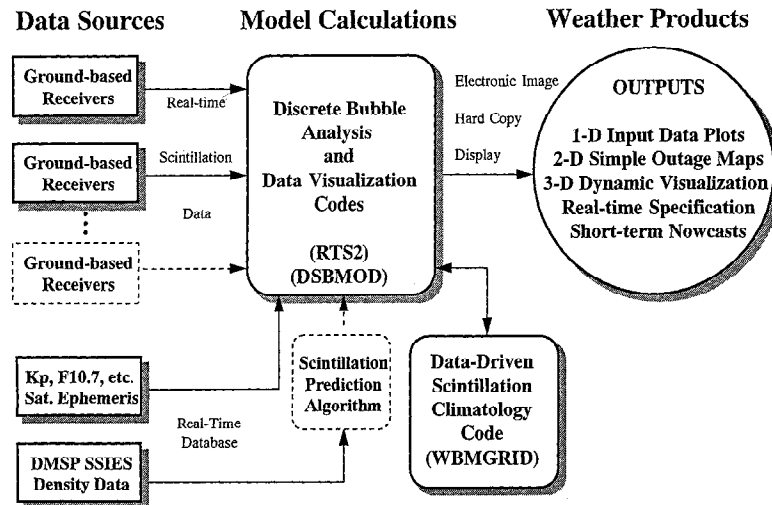


**Figure 8.** Schematic diagram illustrating design of the Scintillation Network Decision Aid (SCINDA). SCINDA ingests geophysical parameters and scintillation data from ground-based receivers to generate a variety of real-time scintillation specification and weather forecast products for operational users. Features not currently implemented but anticipated in the near future are shown with dotted lines.

signal intensity and compute scintillation index  $S_4$  and zonal irregularity drift every 90 s. The data are then retrieved automatically in near real-time via the Internet by the remote SCINDA operator. At the operator terminal the observed parameters are combined with an empirical model of equatorial bubble dynamics in order to generate three-dimensional maps of irregularity structures and related weather products for operational users.

An example of one such map is shown in Plate 1a, where the observed bubbles appear as wedge-shaped features extended north-south along the direction of the magnetic field. The latitudinal extent is determined by the time and location of scintillation detection. When scintillations are first detected at Ancon near the magnetic equator, an irregularity structure is initiated at a nominal altitude of 300 km and propagated upward with a drift speed of  $50 \text{ m s}^{-1}$ . The rising structure is continuously mapped symmetrically north-south along the magnetic field lines and, as a result, the latitude extent of the disturbance increases. The maximum extent is dictated by the measurements at the southern receiver site in Chile. If scintillations are not observed there, as in Figure 3b, the structures are terminated equatorward of the station; the westernmost feature depicted in Plate 1a is a graphic example of one such equatorially localized disturbance. Otherwise, the structure is allowed to propagate to approximately  $\pm 17^\circ$  magnetic lati-

tude, slightly poleward of the nominal location of the equatorial anomaly.

The longitudinal separation of the bubbles shown in Plate 1a results from a combination of the temporal variation of scintillation and the zonal drift velocity of the density irregularities. Structures are initiated at the longitude where scintillations are detected and then propagated at the observed zonal drift velocity, normally eastward at about  $100 \text{ m s}^{-1}$ . Because the kilometer-scale irregularities responsible for 250-MHz scintillation can persist for several hours, the structures can drift hundreds of kilometers before fully decaying. In the present model the eastward drift of features arising from scintillations observed on a western satellite link is constrained by observations near the same latitude on the east link point, some 800 km downstream. The features from the west terminate instantaneously as they reach the east link, where new features are simultaneously generated based on the current observations. If, in fact, the structures created to the west are actually drifting across the east link, this seemingly abrupt transition in the model is essentially transparent in the visualization scheme, as the east link observations will generate new features at the precise moment and location where the inbound features from the west are destroyed. No measurement constraints can be placed on structures spawned by east link observations, however, and they are assumed to decay grad-

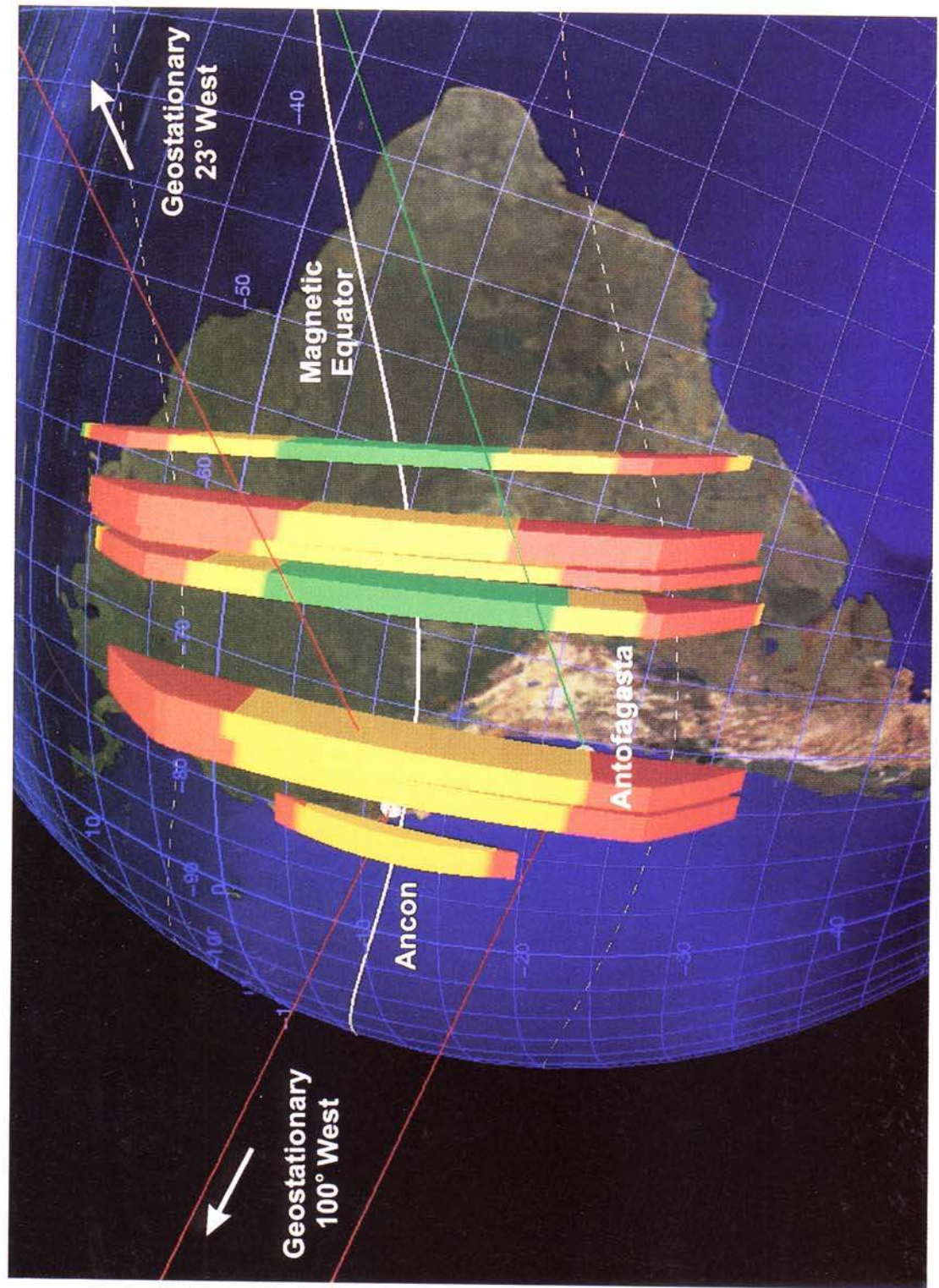


**Plate 1a.** Three-dimensional visualization of equatorial scintillation bubbles observed by SCINDA in October 1996. The system updates the visualization dynamically four times per hour. Bubble amplitude, location, growth, and decay are determined by an empirical model driven by real-time observations of scintillation intensity and zonal drift. Ray paths from the observing stations at Ancon and Antofagasta to geostationary satellites at 100°W and 23°W are color-coded red when they are scintillating and green when they are unperturbed.



ually over a 5-hour period or rapidly within 30 min of local sunrise, whichever occurs sooner. In the absence of real-time drift velocity measurements, climatological drift speeds, matched to the last observed values and current geophysical conditions, are used to connect the scintillation bubbles.

Scintillation intensity is displayed using a simple green-yellow-red color map for ease of interpretation by the operator. The scintillation levels which correspond to each color may be selected by the operator in terms of either  $S_4$  value or specified percentile fade depth in decibels. In Plate 1a the green-yellow-red features represent  $S_4 \leq 0.3$ ,  $0.3 < S_4 \leq 0.6$ , and  $S_4 > 0.6$ , respectively, which correspond to 99 percentile fade levels of  $<6$  dB,  $6-12$  dB, and  $>12$  dB [Whitney, 1974]. The strength of the scintillation is enhanced around the anomaly location at  $15^\circ$  magnetic latitude following the considerations adopted in the improved WBMOD scintillation model [Secan *et al.*, 1995]. Indeed, an efficient, data-driven version of the improved model, known as WBMGRID, has been developed within SCINDA for the purpose of generating better scintillation weather products for operational users.

The two-dimensional outage forecast map shown in Plate 1b represents the primary user product routinely generated by SCINDA. On the basis of current observations of scintillation activity, the map effectively provides up to a 3-hour forecast of communication outage regions to a specific satellite which can be readily understood by any satellite communication user. Satellite link selection can be entered manually or selected graphically from an extensive list with current ephemeris elements. Two distinct types of information are displayed on the map; following the tropospheric severe weather analogy, they are denoted "warning" areas and "watch" areas. Warning areas are based on the projected location of actual observed scintillation structures, while watch areas represent the general probability of outage within the region.

To calculate accurate warning areas, the  $S_4$  values of the observed scintillation features are first converted to the integrated strength of turbulence parameter,  $CkL$ , corresponding to the observation geometry [Secan *et al.*, 1987, 1995]. The locations of observed scintillation features are projected ahead in time using the climatological zonal drift speeds matched to the most recent observed velocities, subject to the irregularity lifetime constraints described above. The anticipated velocity for the time of the

forecast, indicated along the magnetic equator, is included on the plot to provide an estimate of future drift rates to the user. Once the locations are established, the  $CkL$  values are then reconverted to  $S_4$  values using the propagation geometry dictated by the bubble's shadow on the ground projected from the selected satellite. Given a map of the projections, users on the ground can readily assess the anticipated propagation conditions to the satellite from any location within the satellite's footprint on the Earth's surface.

Watch areas are derived by adjusting climatological activity levels to be consistent with current observed levels, and then running the adjusted climatology model, WBMGRID, for the desired time period. This provides a powerful tool for expanding specification beyond the region of actual observations, particularly to the west of ground-based sensors where meaningful predictions would be otherwise impossible due to the eastward drift of observed irregularity features. Scintillation intensity in both the watch and warning areas is displayed using the same simple three-color mapping scheme employed in the three-dimensional view. If the operator sets the color map thresholds properly for a given user, the red-yellow-green areas can be immediately interpreted as regions of severe, moderate, and little effect on his specific system, respectively. Watch areas are delineated further by the crosses and open circles seen in Plate 1b. This facilitates ready differentiation between watch and warning areas and is even effective when faxing black-and-white hard copies to remote users.

## Summary

We have used multistation, multifrequency observations of equatorial scintillation to demonstrate the extreme variability of the occurrence, intensity, and dynamics of scintillating regions. At high latitudes the intense ionospheric disturbances are usually examined by following the trail of energy from the Sun. We have shown that in sharp contrast to this, the equatorial scintillation activity attains its maximum level during magnetically quiet conditions. The complex thermosphere-ionosphere interactions that cause the ionosphere to become unstable continue to be studied in the context of new mechanisms and refined models [Haerendel and Eccles, 1992; Crain *et al.*, 1993] as well as observational results obtained by radio, radar, and optical techniques [Basu *et al.*, 1996; Weber

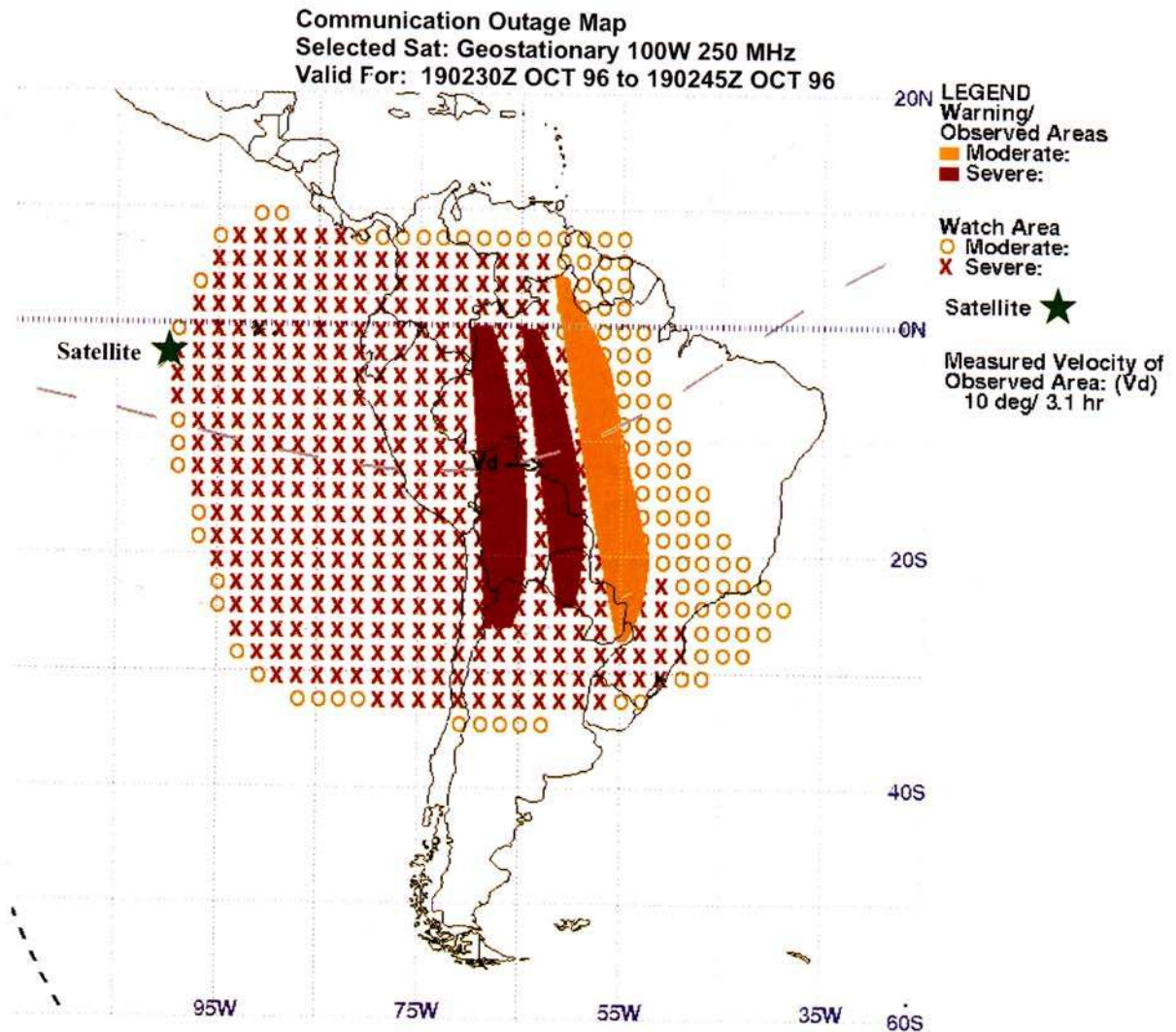


**Plate 1b.** Two-dimensional forecast communication outage map showing scintillation “warning” (observations) and “watch” (model) areas over much of South America for a VHF link to a geostationary satellite at 100°W longitude. The simple red-yellow-green color scheme corresponds to severe, moderate, and little effect, respectively, on the communication system employed.



*et al.*, 1996]. In spite of these advances, the variability of scintillation remains an unresolved problem.

We have also used scintillation statistics and case studies to demonstrate that once the scintillating regions are formed, they evolve and convect in a well-ordered manner. The Scintillation Network Decision Aid (SCINDA) has been developed in this framework. In its current form, SCINDA provides valuable diagnostic information that serves both the scientific research and operational communities. The maps of scintillating regions in space and time provided by SCINDA will define the framework for the investigations of the irregularity onset and evolution. Operational users will benefit from the real-time specification of scintillation activity; this information can be used to exploit, in a timely manner, alternate communication and navigation assets and reduce resources allocated to troubleshooting disruptions caused by scintillation. SCINDA will also serve as a unique tool for the validation of the coupled ionospheric scintillation model, a physics-based model currently under development at Phillips Laboratory.

Several extensions to the existing system are being planned in the near future that include the deployment of an additional latitudinally dispersed station to reproduce the north-south asymmetry of scintillation; the implementation of an algorithm to predict globally the onset of scintillation based on the ion density data from the SSIES sensor on DMSP satellites [Sultan, 1996]; and the extension of the frequency and spatial coverage of the observations by the addition of GPS receivers capable of recording amplitude and phase scintillations. Overall, by implementing new algorithms, by improving the model through continued validation, and by extending the system capability to GPS frequencies, SCINDA will partially fulfill the goal of the National Space Weather Program to globally specify and forecast ionospheric scintillation.

**Acknowledgments.** We thank Sunanda Basu for useful discussions and a careful reading of the manuscript. We gratefully acknowledge the cooperation of the personnel of the Instituto Geofísico del Perú in operating the Ancon Observatory. The work at Phillips Laboratory was partially supported by the Air Force Office of Scientific Research under task 2310G9. The work at Boston College was partially supported by NSF grant ATM-9202350 and Phillips Laboratory contract F19628-90-K-0007.

## References

- Aarons, J., The role of the ring current in the generation or inhibition of equatorial *F*-layer irregularities during magnetic storms, *Radio Sci.*, 26, 1131, 1991.
- Aarons, J., The longitudinal morphology of equatorial *F*-layer irregularities relevant to their occurrence, *Space Sci. Rev.*, 63, 209, 1993.
- Aarons, J., and S. Basu, Ionospheric amplitude and phase fluctuations at the GPS frequencies, in *Proceedings of ION GPS-94*, pp. 1569–1578, Inst. of Navig., Arlington, Va., 1994.
- Aarons, J., M. Mendillo, and R. Yantosca, GPS phase fluctuations in the equatorial region during sunspot minimum, *Radio Sci.*, this issue.
- Anderson, D. N., and G. Haerendel, The motion of depleted regions in the equatorial ionosphere, *J. Geophys. Res.*, 84, 4251, 1979.
- Basu, Su., and S. Basu, Equatorial scintillations: Advances since ISEA-6, *J. Atmos. Terr. Phys.*, 47, 753, 1985.
- Basu, S., E. MacKenzie, and Su. Basu, Ionospheric constraints on VHF/UHF communications links during solar maximum and minimum periods, *Radio Sci.*, 23, 363, 1988.
- Basu, S., G. J. Bishop, and J. Larson, Turbulence in the upper atmosphere: Effects on systems, *AGARD Conf. Proc.*, AGARD-CP-573, 24A-1–24A-9, 1995.
- Basu, S., et al., Scintillations, plasma drifts, and neutral winds in the equatorial ionosphere after sunset, *J. Geophys. Res.*, 101, 26,795, 1996.
- Crain, D. J., R. A. Heelis, G. J. Bailey, and A. D. Richmond, Low-latitude plasma drifts from a simulation of the global atmospheric dynamo, *J. Geophys. Res.*, 98, 6039, 1993.
- Farley, D. T., E. Bonelli, B. G. Fejer, and M. F. Larsen, The prereversal enhancement of the zonal electric field in the equatorial ionosphere, *J. Geophys. Res.*, 91, 13,723, 1986.
- Fejer, B. G., Low latitude electrodynamic plasma drifts, *J. Atmos. Terr. Phys.*, 53, 677, 1991.
- Fejer, B. G., E. R. dePaula, S. A. Gonzalez, and R. F. Woodman, Average vertical and zonal *F*-region plasma drifts over Jicamarca, *J. Geophys. Res.*, 96, 13,901, 1991.
- Haerendel, G., Theory of equatorial spread-*F*, report, Max-Planck-Inst. für Extraterr. Phys., Garching bei München, Germany, 1973.
- Haerendel, G., and J. V. Eccles, The role of the equatorial electrojet in the evening ionosphere, *J. Geophys. Res.*, 97, 1181, 1992.
- Heelis, R. A., P. C. Kendall, R. J. Moffett, and D. W. Windle, Electrical coupling of the *E* and *F* regions and its effect on *F* region drifts and winds, *Planet. Space Sci.*, 22, 743, 1974.
- Kelley M. C., *The Earth's Ionosphere*, Int. Geophys. Ser., vol. 43, p. 71, Academic, San Diego, Calif., 1989.
- McClure, J. P., W. B. Hanson, and J. H. Hoffman, Plasma

- bubbles and irregularities in the equatorial ionosphere, *J. Geophys. Res.*, **82**, 2650, 1977.
- Maruyama, T., and N. Matuura, Longitudinal variability of annual changes in activity of equatorial spread-*F* and plasma bubbles, *J. Geophys. Res.*, **89**, 10,903, 1984.
- Ossakow, S. L., Spread-*F* theories—A review, *J. Atmos. Terr. Phys.*, **43**, 437, 1981.
- Ossakow, S. L., and P. K. Chaturvedi, Morphological studies of rising equatorial spread *F* bubbles, *J. Geophys. Res.*, **83**, 2085, 1978.
- Ossakow, S. L., S. T. Zalesak, B. E. McDonald, and P. K. Chaturvedi, Nonlinear equatorial spread-*F*: Dependence on altitude of the *F*-peak and bottomside background electron density gradient scale length, *J. Geophys. Res.*, **84**, 17, 1979.
- Ott, E., Theory of Rayleigh-Taylor bubbles in the equatorial ionosphere, *J. Geophys. Res.*, **83**, 2066, 1978.
- Rishbeth, H., Polarization fields produced by winds in the equatorial *F* region, *Planet. Space Sci.*, **19**, 357, 1971a.
- Rishbeth, H., The *F* layer dynamo, *Planet. Space Sci.*, **19**, 263, 1971b.
- Rishbeth, H., The *F*-region dynamo, *J. Atmos. Terr. Phys.*, **43**, 387, 1981.
- Scannapieco, A. J., and S. L. Ossakow, Nonlinear equatorial spread-*F*, *Geophys. Res. Lett.*, **3**, 451, 1976.
- Secan, J. A., E. J. Fremouw, and R. E. Robins, A review of recent improvements to the WBMOD ionospheric scintillation model, in *Effects of the Ionosphere on Communication, Navigation, and Surveillance Systems*, edited by J. Goodman, pp. 607–617, U.S. Govt. Print. Off., Springfield, Va., 1987.
- Secan, J. A., R. M. Bussey, E. J. Fremouw, and S. Basu, An improved model of equatorial scintillation, *Radio Sci.*, **30**, 607, 1995.
- Sekar, R., R. Suhasini, and R. Raghavarao, Effects of vertical winds and electric fields in the nonlinear evolution of equatorial spread-*F*, *J. Geophys. Res.*, **99**, 2205, 1994.
- Sridharan, R., D. Pallam Raju, and R. Raghavarao, Precursor to equatorial spread-*F* in OI 630.0-nm dayglow, *Geophys. Res. Lett.*, **21**, 2797, 1994.
- Sultan, P. J., Satellite signatures of the global occurrence morphology of equatorial spread-*F*, in *Proceedings of the Ionospheric Effects Symposium*, pp. 287–292, Natl. Tech. Inf. Serv., Springfield, Va., 1996.
- Tsunoda, R. T., Time evolution and dynamics of equatorial backscatter plumes, 1, Growth phase, *J. Geophys. Res.*, **86**, 139, 1981.
- Tsunoda, R. T., R. C. Livingston, J. P. McClure, and W. B. Hanson, Equatorial plasma bubbles: Vertically elongated wedges from the bottomside *F*-layer, *J. Geophys. Res.*, **87**, 9171, 1982.
- Valladares, C. E., W. B. Hanson, J. P. McClure, and B. L. Cragin, Bottomside sinusoidal irregularities in the equatorial *F*-region, *J. Geophys. Res.*, **88**, 8025, 1983.
- Valladares, C. E., S. Basu, R. Sheehan, H. Kuenzler, and J. Espinoza, The multi-instrumented studies of equatorial thermosphere aeronomy scintillation system: Climatology of zonal drifts, *J. Geophys. Res.*, **101**, 26,839, 1996.
- Weber, E. J., S. Basu, G. Bishop, T. Bullett, H. Kuenzler, P. Ning, P. Sultan, C. Valladares, and J. Araye, Equatorial plasma depletion precursor signatures and onset observed at 11° south of the magnetic equator, *J. Geophys. Res.*, **101**, 26,829, 1996.
- Whitney, H. E., Notes on the relationship of scintillation index to probability distributions and their uses for system design, *Rep. AFCRL-TR-74-0004*, Phillips Lab., Hanscom Air Force Base, Mass., 1974.
- Woodman, R. F., and C. La Hoz, Radar observations of *F*-region equatorial irregularities, *J. Geophys. Res.*, **81**, 5447, 1976.
- S. Basu, K. M. Groves, H. Kuenzler, M. Smitham, and E. J. Weber, Phillips Laboratory, PL/GPI, 29 Gernier Street, Hanscom Air Force Base, MA 01731. (e-mail: santimay@aol.com; groves@plh.af.mil)
- M. J. Kendra, W. J. McNeill, and D. W. Moonan, Radex Incorporated, 3 Preston Court, Bedford, MA 01730. (e-mail: mcneil@plh.af.mil)
- E. MacKenzie, R. Sheehan, and C. E. Valladares, Institute for Scientific Research, Boston College, 140 Commonwealth Avenue, Chestnut Hill, MA 02167. (e-mail: cesar@dlws7.bc.edu)
- P. Ning, Keo Consultants, 27 Irving Street, Brookline, MA 02146. (e-mail: ning@ai.mit.edu)
- J. A. Secan, Northwest Research Associates, 14508 NE 20th Street, Bellevue, WA 98007. (e-mail: jim@nwra.com)

(Received November 7, 1996; revised February 25, 1997; accepted March 20, 1997.)